Diyala Journal of Engineering Sciences

Journal homepage: https://djes.info/index.php/djes

ISSN: 1999-8716 (Print); 2616-6909 (Online)

A Data-Driven Multiscale Nonlinear Segmentation Framework for Silicosis Detection Using Machine Learning

N. Shivaanivarsha*, P. Kavipriya

Department of Electronics and Communication Engineering Sathyabama Institute of Science and Technology, Chennai, India.

ARTICLE INFO

Article history:
Received: 11/03/2026.
Revised:05/07/2026.
Accepted: 26/08/2026
Available online: 15/09/2026

Keywords:
Silicosis detection
Nonlinear scale space
Multiscale image segmentation
Machine learning
Lung imaging

ABSTRACT

Early-stage silicosis is challenging to identify since lung alterations might appear as micronodules, distorted parenchymal patterns, or fibrotic changes. In this paper, we introduce a nonlinear multiscale image segmentation framework, with machine-learning classification, for computer-aided assessment of silicosis. The proposed method combines nonlinear total-variation (TV)-flow scale-space construction, hierarchical region merging, data-driven rgion pruning, and region-level machine learning classification. In contrast to traditional image-based classifiers, the approach generates interpretable lung subregions featuring micronodular and fibrotic lesions prior to classification. A nonlinear scale-space stack is constructed by using diffusion-based partial differential equations while maintaining lesion boundaries at different anatomical scales. The resulting structures are connected via a hierarchical region tree, and a data - driven pruning procedure is employed to prune unstable or non-anatomical regions within each path without any manual intervention. Intensity, shape, texture, and multiscale features are extracted from the retained regions and then used for supervised classification. The study consisted of 64 subjects and 286 HRCT slices. The segmentation-based method performed 9–11 % better in classification accuracy compared to the single-scale approaches or non-oriented features and achieved ~ 92 % sensitivity in detecting early stage silicosis. The framework also showed better edge preservation, less over segmentation, and practical computational efficiency. These results motivate the continued investigation of the approach as an interpretable computer-aided silicosis assessment framework.

1. INTRODUCTION

Prolonged inhalation of respirable crystalline silica can cause the progressive fibrotic lung disease silicosis, which is an important public health problem worldwide [1]. Early diagnosis is difficult since chest CT images may manifest as tiny micronodular opacities, irregular parenchymal patterns and/or extensive parenchymal fibrosis [2], [3]. Precise segmentation of those abnormal lung areas is also necessary, because the classification accuracy is strongly influenced by the quality of the extracted image features [4]–[8].

Conventional segmentation algorithms such as thresholding, clustering, watershed, active-contour techniques usually fail when the lung tissue is nonhomogeneous or small nodules are surrounded by large fibrotic opacities. Deep-learning methods for pneumoconiosis and associated lung diseases have significantly progressed, but a large number function as image-level classifiers with limited anatomical interpretability [5]–[10]. Furthermore, the presence of low-dose CT noise, weak lesion boundaries, and the multiscale characteristic of silicosis also continue to pose significant challenges for precise automated diagnosis [8], [9].

In this work, we propose a data-driven nonlinear multiscale segmentation strategy for silicosis detection to tackle the aforementioned problems. It is a method that employs total variation flow for creating an edge-preserving scale space representation, builds a hierarchical region tree at different scales, and extracts region based intensity, shape, texture and multiscale features for machine learning classification. The goal is to enhance the localization of lesions, to reduce over-segmentation and to give interpretable regions for diagnosis of silicosis.

*Corresponding author's E-mail: varsha.ece@sairam.edu.in | ORCID: 0000-0003-3532-6038
DOI: 10.24237/djes.2026.19310

The novelty of this work goes beyond hierarchical region-tree construction. Our main novelty lies hence in the overall pipeline, a complete silicosis-specific one, that combines non-linear TV-flow scale-space based region evolution, edge-aware region evolution, hierarchical linking using spatial overlap and gray-level similarity, data-driven region pruning, and region-level ml classification.

This enables detection of micronodules and fibrotic patterns with diagnostic classification. Instead of a general-purpose hierarchical segmentation method, the proposed pipeline is tailored and validated for silicosis CT analysis to maximize preservation of lesions of an early stage and robustness to simulated low-dose noise. The main contributions of this paper are: (1) denoising CT images with TV-flow based nonlinear scale-space model while maintaining small and weak silicotic nodules, (2) a powerful region-linking scheme strictly backed by edge-aware pruning is capable of efficiently linking pertinent lung regions without introducing large error due to merging normal parenchyma with pathological tissue, (3) intensity, shape, texture, and multiscale region-level features used for ml-based silicosis classification, and (4) a series of experiments on CT volumes against classical segmentation approaches and representative AI baselines [11]–[14] evaluates the proposed framework.

The rest of this paper is organized as follows. Section 2 gives a short review of related methods in silicosis detection and medical image segmentation. The linear scale-space segmentation framework is presented in Section 3, the nonlinear multiscale TV-flow approach is presented in Section 4. The experimental results and performance evaluation are given in Section5. Section 6 generalizes the framework to multichannel images. In Section 7, clinical implications and future work are discussed, followed by conclusions in Section 8.

2. LITERATURE REVIEW

During the past 10 years, there have been significant advances in the ability of artificial intelligence (AI), in particular deep learning (DL), to perform automated analysis of images in the field of thoracic medical imaging (chest radiographs, CT and histopathological images). These achievements have been leveraged for early detection, classification, prognosis prediction, and severity assessment of several lung diseases, such as pneumoconiosis, lung cancer, COVID-19, silicosis, and other thoracic diseases.

Devnath et al. [14] presented a deep-ensemble architecture to detect pneumoconiosis in chest X-ray images of the coal workers and showed enhanced classification reliability. Davri et al. [15] reviewed the current deep-learning techniques applied to lung-cancer diagnosis and identified variability among datasets, limited interpretability, and large annotated datasets as a major barrier for development. Balcı et al. [16] introduced a deep-learning approach for lung-nodule classification and achieved an enhanced recognition of lung lesions. Bhosale and Patnaik [17] summarized the CNN-based COVID-19 diagnostics and highlighted the data-quality related concerns and reproducibility issues. Yi et al. [18] assessed the performance of radiologists in detecting silicosis on HRCT and found that even experts have difficulty in diagnosis. Sharma et al. [19] proved that transfer learning can be feasible for silicosis detection in the presence of a few labeled medical images. Zhang et al. [20] verified that deep learning for pneumoconiosis screening with digital chest radiography is viable. Anderson et al. [21] showed that deep-learning-based chest X-ray analysis has the ability to accurately identify a wide range of thoracic diseases and considerably enhances the diagnostic performance of physicians, indicating the clinical usefulness of automated interpretation of lung images. Liu et al. [22] introduced a multistage deep-learning framework for the diagnosis and staging of pneumoconiosis and Priego-Torres et al. [23] proposed an image-level deep-learning method for the screening and staging of engineered-stone silicosis. An overview of these studies positive and adverse findings is presented in Table 1.

Table 1. Comparison of silicosis and pneumoconiosis detection studies reported previously.

Ref.	Method	Modality	Main reported finding	Identified limitation
[24]	Deep-learning pneumoconiosis screening based on CNN	Digital chest radiography	Obtained results with higher accuracy, 94.7% AUC at 100% sensitivity for the classification of pneumoconiosis	System was designed for radiograph-level screening and does not provide HRCT lesion-level segmentation
[25]	YOLO-CXR lesion detection framework	Chest X-ray	Localized multiple small thoracic opacities in chest radiographs	Not being developed specifically for silicosis and ignoring 3D CT lesion patterns.
[26]	A Systematic Review and Meta-Analysis of Diagnostic Biomarkers for Silicosis	Clinical/biological markers of disease	The pooled sensitivity and specificity was 0.84 and 0.83 respectively, with an AUC of 0.90	None of these performed lung-image segmentation or lesion localization; biomarker performance exhibited heterogeneity across studies

[27]	ExpertNet deep expert-consultation network	Radiography of the chest	Obtained 89% accuracy, 81.3% precision, 79.5% recall, 80.1% F1-measure and 95.5% AUC for the staging of pneumoconiosis	dealing with image-level pneumoconiosis staging rather than silicosis-specific HRCT lesion segmentation
[28]	Deep texture encoding with contrastive learning	Chest X-ray	The tail-labelled and disc-based FC representation can capture the discriminative radiographic texture representations of pneumoconiosis, and thus is able to obtain an improved pneumoconiosis staging result	Tested on a rather small dataset, and did not address CT-based regional abnormalities.
[29]	Multimodal fusion of chest radiographs and blood biomarkers	Chest X-ray and clinical biomarkers	Silicosis staging enhancement by late- and hybrid-fusion modalities	Needed multiple input modalities and did not give lesionâ€‘level CT segmentation/localization.
[14]	Deep ensemble classification	Chest X-ray	Enhanced the reliability of the classification of pneumoconiosis in coal workers.	Mainly gave image-level predictions and did not locate specific abnormal lung regions.
[18]	A radiologist HRCT diagnostic evaluation	High-resolution CT	Showed diagnostic significance of HRCT in differentiating silicotic from non-silicotic nodules.	Demonstrated considerable diagnostic challenge and variability among observers, including experts.
[19]	Classification based on transfer learning	Chest radiograph or thoracic image data	Better identification of silicosis with limited labeled data.	Was oriented to global classification, bringing the anatomical interpretability to a limited extent.
[20]	Screening for pneumoconiosis using deep learning	Digital chest radiography	Navigated the complexity of occupational-lung-disease to demonstrate the potential for automated, scalable screening	Was not intended to identify micronodules, irregular opacities, or fibrotic lesions at the level of the CT-region.
[22]	Multistage deep-learning diagnosis and staging method	Chest X-ray	Facilitated automated diagnosis of pneumoconiosis and prediction of disease-stage	Concentrated on diagnosis and staging, not on explicit HRCT lesion segmentation.
[23]	Image-level deep-learning framework for engineered-stone silicosis	Chest X-ray	Automated screening and staging of engineered-stone-associated silicosis	Did not include nonlinear multiscale CT analysis or interpretable lesion characterization at the region level.

As can be seen from Table 1, the majority of the existing work is related to chest-radiograph-based screening, disease level classification, staging, or multimodal fusion with clinical biomarkers. These methods illustrate the promise of AI in occupational lung-disease evaluation, but they typically yield global image-level decisions and provide little information on the location, morphology, and multiscale behaviors of individual silicotic lesions. HRCT-based segmentation of weak micronodular opacities, abrupt parenchymal texture alteration, and progressive massive fibrosis (PMF) has scarcely been attempted in the literature under an integrated framework. Also, standard deep-learning classifiers have been known to require large amount of labeled datasets and might not explicitly preserve faint lesion boundaries or highlight anatomically meaningful regions that contribute to the diagnostic decisions. Thus, an interpretable HRCT scheme which integrates edge-preserving nonlinear scale-space construction, hierarchical region linking, data-driven region pruning, and region-level machine-learning classification is still in demand from the research viewpoint. This research was meant to fill that void.

3. DETECTION OF SILICOSIS BY LINEAR SCALE-SPACE SEGMENTATION

In the absence of background information on lung nodules or fibrotic patterns in a CT scan, an unbiased visual front end [6], [7] comes in handy. It is helpful in preserving important attributes including linearity, spatial-shift invariance, isotropy, and scale-invariance. The linear scale-space theory allows a multiscale description of lung structure while satisfying these properties [7], [19].

3.1. Linear Scale Space in Lung Imaging

The linear scale-space representation is formed by combining a lung computed tomography image I x y with the images L x y; ð, which are computed with σ

the Gaussian diffusion kernel as in Equation 1, where σ is the standard deviation of the kernel.

$$\frac{\partial L}{\partial \sigma} = \nabla^2 L, L(x, y; 0) = I(x, y) \quad (1)$$

The parameter σ slowly increases to enhance the ability to find structures of different scales. This is also achieved with a convolution with a Gaussian kernel (Equations 2-3).

$$L(x, y; \sigma) = I(x, y) * G(x, y; \sigma) \quad (2)$$

$$L(x, y; \sigma) = \frac{1}{2\pi\sigma^2} e^{-\frac{x^2+y^2}{2\sigma^2}} \quad (3)$$

A Gaussian kernel is used to smooth the image and provide a more detailed representation of the large-scale features (such as silicotic nodules) and noise. Besides, the derivatives of L are solutions to the heat equation and can be used to analyse edges and features at various scales (Equation 4).

$$\frac{\partial}{\partial \sigma}\left(\frac{\partial L}{\partial x}\right) = \nabla^2 \left(\frac{\partial L}{\partial x}\right) \quad (4)$$

This is an important function to locate the edges and fibrotic limits at different scales.

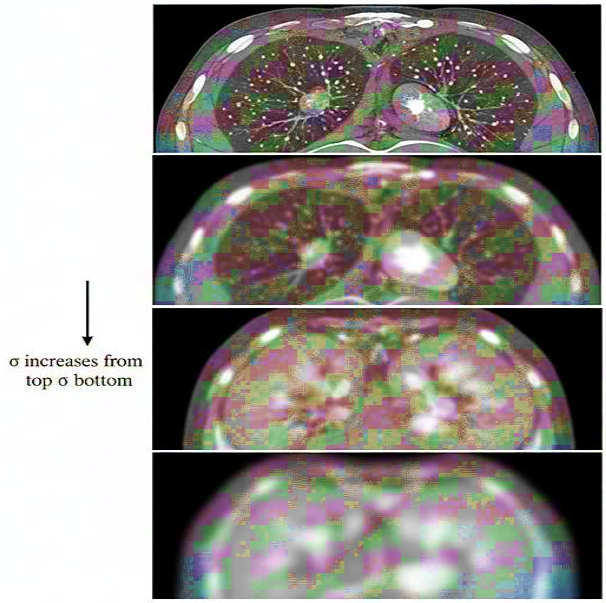

Figure 1. Linear scale-space stack of a lung CT slice (σ increases from top to bottom).

Figure 1 illustrates a linear scale-space stack of a lung computed tomography (CT) slice. The scale parameter σ varies from top to bottom, resulting in the smoothing becoming increasingly stronger at larger scales. Small nodules are highlighted at fine scales while large regions of fibrosis are still visible at coarse scales.

3.2. Segmentation Process: Linking Through Scale

The fibrotic patterns of silicosis may be in scale space, represented as hierarchies. The algorithm starts from fine details like isolated small nodules and then follows structures through a series of coarser iso-intensity scales. This procedure produces a multiscale hierarchical organization of pixels. Lung-tissue pixels are connected across scales in Figure 2 (b) and 2 (c), and fine-scale details are linked to coarser representations. Circular windows centered on each pixel define parent-child relationships, the size of the window is a function of σ. Within this window, the pixel presenting the most similar intensity-gradient profile is chosen as the parent node.

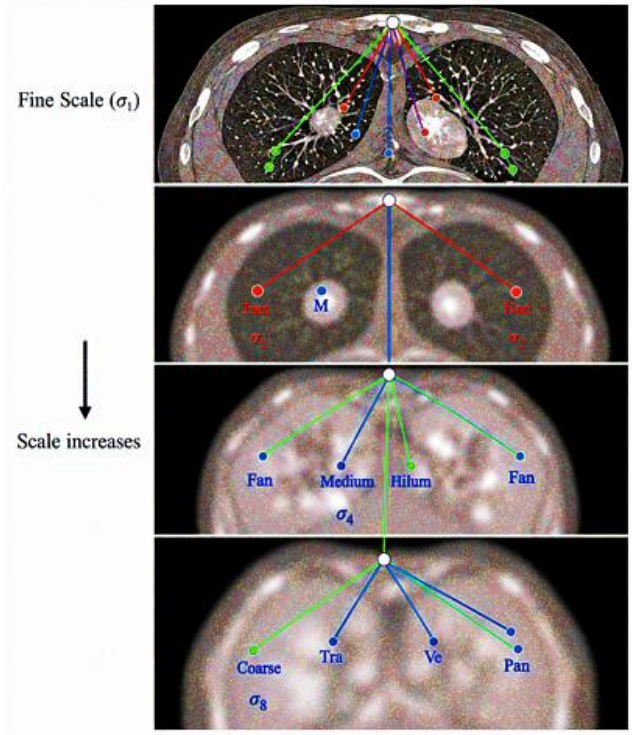

Figure 2. Hierarchical linking of lung tissue pixels across scales.

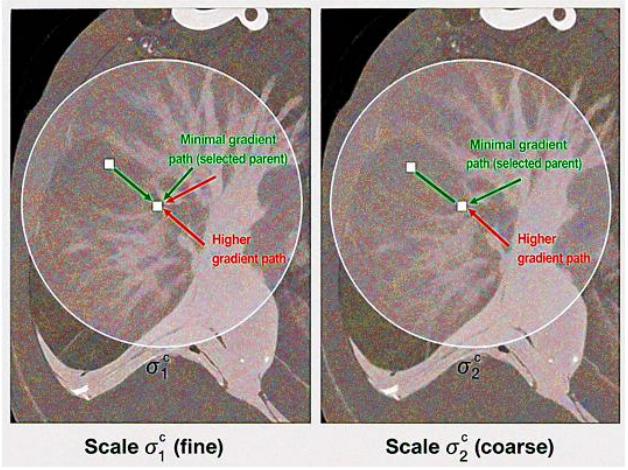

Figure 3. Search window for associating the child pixels with parent nodes in lung CT.

Each segment represents a group of pixels related to a root node of the tree and representing a fibrotic region or nodule as in Figure 3. The stopping scale controls the segmentation result and the largest structure which can be detected.

3.3. Supervising Segmentation with Multiscale Edges

These direct connections can also result in inappropriate regions linking together, creating false connections. To this end, we introduce edge supervision with multi-scale edge detection.

- Scale through edges: Second derivatives of Gaussian detect boundaries of nodules and fibrosis at various scales.

- Edge-guided linking: The search area is transformed into a common coordinate system so as to ensure that the parent and child pixels belong to the same area or blob. Edges with links are deleted.

Multiscale DoG edge detection in lung CT is shown in Figure 4. Figure 5 illustrates the correction of misguided region linking by edge supervision. Silicosis segmentaion is governed by scale, neighborhood linking, edge information, and root-region selection. The scale enables us to detect small nodules at fine scales and large fibrotic regions at coarse scales, whereas the search radius preserves parent-child relationships across scales. Edge supervision prohibits links to cross tissue boundaries, and root-node selection leads to the final segmented diseased regions.

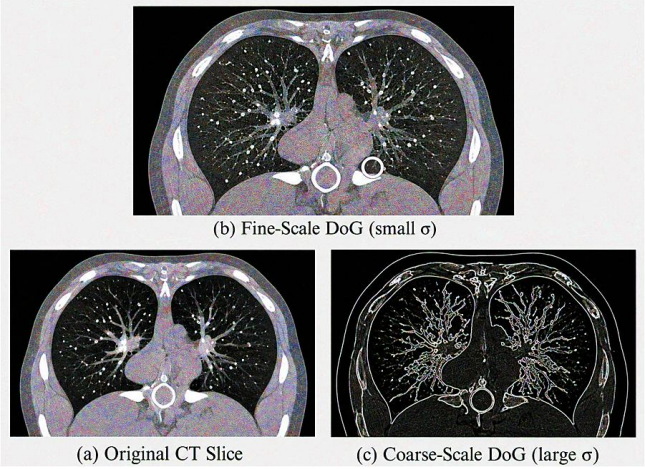

Figure 4. Multi-scale edge detection in lung CT slices using Difference of Gaussians (DOG).

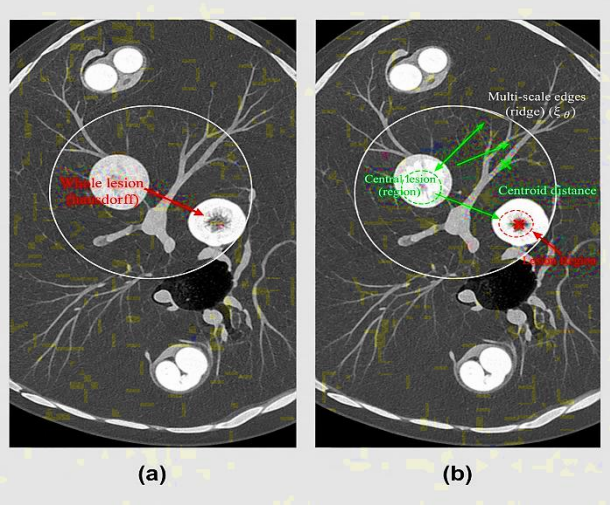

Figure 5. Avoiding wrong linkage using edge supervision. (a) Direct Linking (b) Edge- guided linking

3.4. Segmentation Results

The experiments were conducted on lung computed tomography (CT) image data sets with both early and late stages of silicosis. The two parameters were: edge supervision and stopping scale.

- Edge supervision: the edge information is what prevents separate nodules or regions of fibrosis from being merged. Figure 6 the left subfigure corresponds to segmentation result without edge supervision, while the right subfigure is with edge supervision.
- Scale selection: The stopping scale should be appropriately determined. Small scales are used to see small nodules, and large scales are used to get large fibrotic areas.

Figure 6 demonstrates the comparison without edge guidance (left) and with edge guidance (right) in the segmentation procedure. Edge-guided segmentation can still better maintain the boundary of lesion. The influence of the stopping scale is shown in Figure 7: Smaller stopping scales preserve small structures, coarser scales focus on larger areas. The summary of the edge guided and -unguided segmentation in Figure 8. The Dice score was increased from 0.72 to 0.89, precision from 0.75 to 0.91 and recall from 0.70 to 0.88. The number of regions produced by segmentation was 26, an additional 2 regions were added as compared to the previous 24, indicating a finer separation of pathologically significant regions.

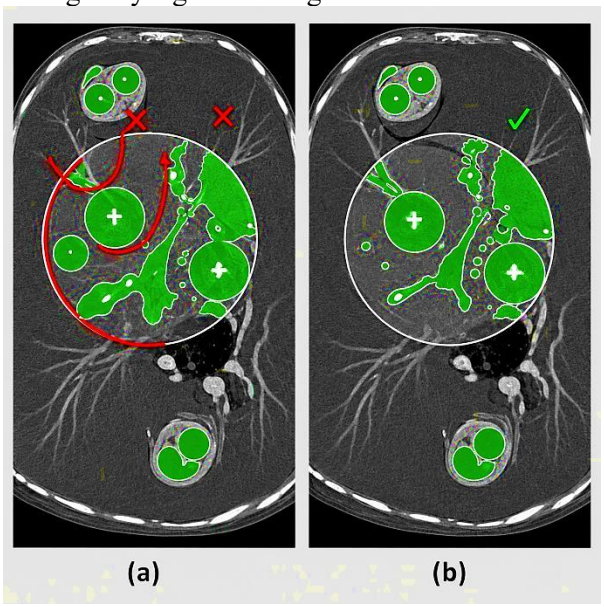

Figure 6. Left: Original segmentation, Right: Segmentation with edge supervision.

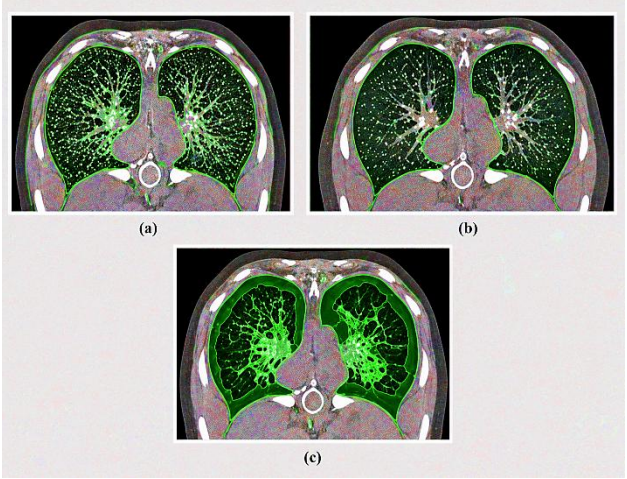

Figure 7. The impact of scaling on the segmentation detail. The original CT slice is shown in (a), the fine Stopping Scale (small σ) is shown in (b), and the coarse-Scale DOG (large σ) is shown in (c).

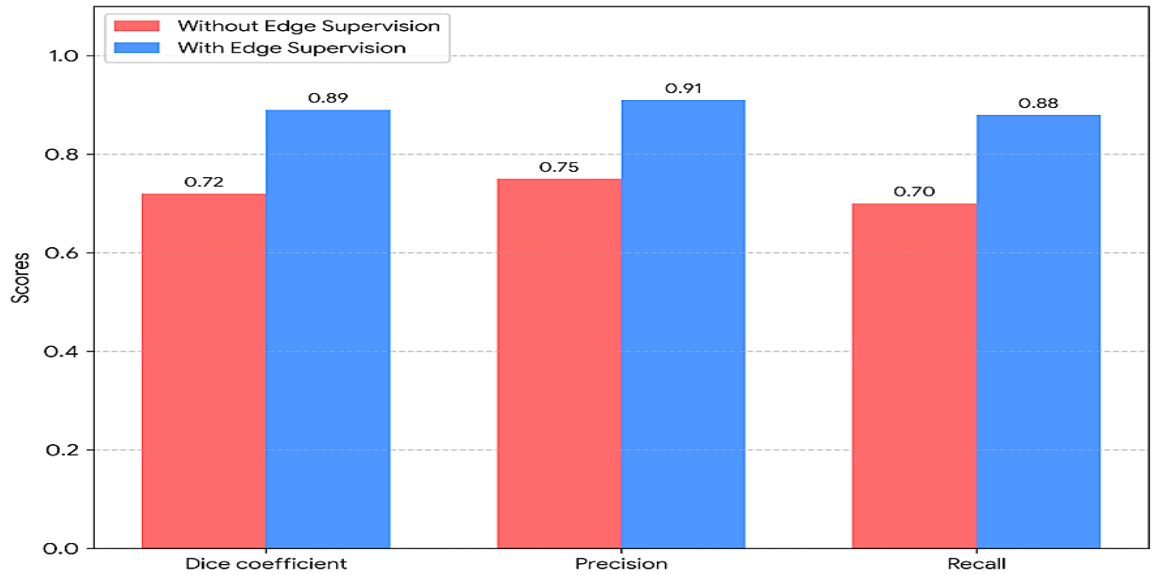

Figure 8. A set of metrics used to evaluate segmentation for silicosis detection.

The findings show that the linear scale-space segmentation with edge supervision is successfully applied to nodular and fibrotic patterns and thus is a valid pre-processing stage for machine-learning classification.

4. NONLINEAR SCALE-SPACE: HANDLING LUNG IMAGE STRUCTURE FOR SILICOSIS DETECTION

Edge supervision enhances pixel linking in lung CT scans, preventing small nodules or fibrotic areas from conglutinating with adjacent tissue. More global and unsupervised strategies rely on nonlinear scale-space models that homogenize regions while preserving coherent structures. Since edge preservation is important to retain silicotic nodules and fibrotic borders, nonlinear scale spaces are ideal for this application.

In medical images, there are basically three widely used models based on nonlinear PDE for image segmentation.

4.1. Perona–Malik Diffusion

The Perona-Malik Diffusion introduces an edge-stopping function (Equation 5):

$$\frac{\partial L}{\partial t} = \mathrm{div}(c(|\nabla L|)\nabla L) \quad (5)$$

where $c(\cdot)$ is an edge-stopping function that controls the amount of smoothing across large gradient values. Therefore, The uniform regions can be smoothed without losing sharpness of high-gradient edges, such as boundaries of nodule or fibrosis.

This process is limited as it relies on a user specified contrast threshold that might not be uniformly applied to all the images. Furthermore, the method may become numerically unstable in areas of large intensity gradients.

4.2. Mean Curvature Motion

When the value of the diffusion coefficient in the gradient direction is set to the gradient value, mean curvature motion (Equation 6) results.

$$\frac{\partial L}{\partial t} = |\nabla L|\mathrm{div}\left(\frac{\nabla L}{|\nabla L|}\right) \quad (6)$$

Our method is designed to diffuse mainly along directions orthogonal to the image gradient. Thus, it can smooth homogeneous regions and preserve edges at the same time. This attribute is particularly important for lung imaging as retaining nodule contours is vital for any useful analysis. As time evolves, small level-set components vanish and this leads to a scale dependent simplification of features as shown in Figures 8–10.

4.3. Total Variation (TV) Flow

The TV-based image processing has shown good noise reduction and preservation of local CT edge informations [12]. In the sense of the proposed method, TV flow can be considered as an edge-preserving nonlinear diffusion process defined via the total variation norm as given in Equation 7.

$$\frac{\partial L}{\partial t} = \mathrm{div}\left(\frac{\nabla L}{|\nabla L|}\right) \quad (7)$$

One of the advantages of the proposed TV-flow model for silicosis detection is that the nodule and fibrosis boundaries remain visible longer than in curvature flow. This preserves structurally significant information which is important for diagnosis and at the same time smooths lung parenchyma and increase contrast between normal and suspicious areas (see Figures 9–12).

The nonlinear diffusion model uses a local coordinate system for the lung CT images as shown in Figure 9. Figure 10 illustrates the use of mean curvature flow for shape smoothing in lung CT scans and the resulting smoothing of the shapes. Figure 11 shows the evolution of level sets for geometric heat flow, and represents the dynamics of the regions. The TV flow application is multi-scale as shown in Figure 12, where the lung nodules and fibrotic regions are preserved. Figure 13 shows TV flow as a function of mean curvature flow, and demonstrates the advantage of TV flow in smoothing the interior of regions while preserving edge integrity.

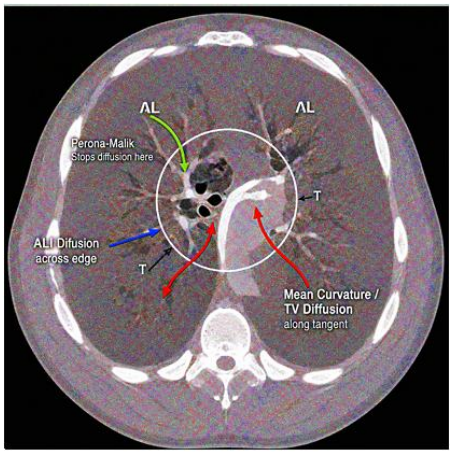

Figure 9. Local coordinate system for nonlinear diffusion.

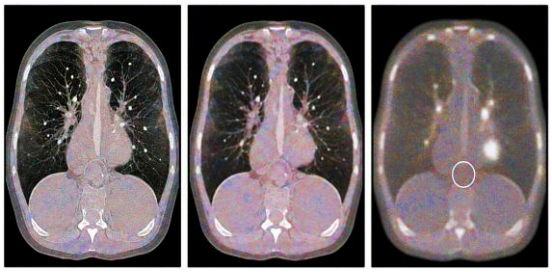

Figure 10. Lung CT slices (mean curvature flow).

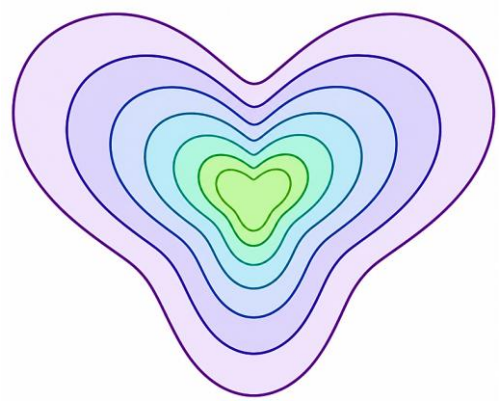

Figure 11. The level sets corresponding to the solution of the geometric heat flow.

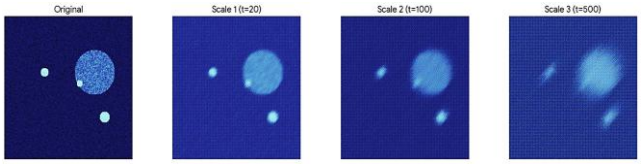

Figure 12. A multi-scale view of flow through TV in a region containing lung nodules and fibrotic areas.

4.4. Multiscale Image Representation for Silicosis

In TV-flow evolution, an image is represented through isolevel sets as introduced in Equation 8.

$$L_\lambda = \{((x,y)|L(x,y) = \lambda)\} \quad (8)$$

These sets have edges as boundaries. They offer a powerful and simple image structure parameterization. The isolevel sets can be naturally nested, and a hierarchical tree of lung regions at multiple scales can be obtained as illustrated in Figure 14.

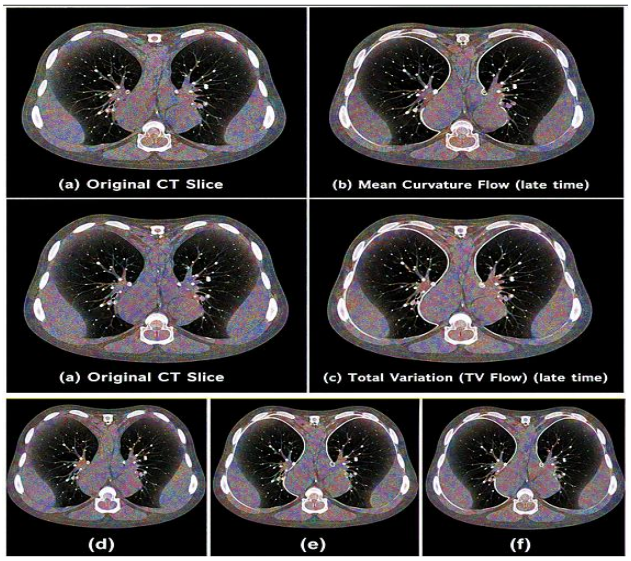

Figure 13. Edges are preserved well in the TV flow compared to the mean curvature flow. (a) Original CT slice, (b) TV flow, and (c) Mean curvature flow.

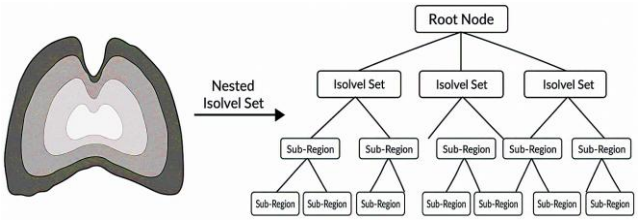

Figure 14. Hierarchical tree of lung regions based on TV flow decomposition.

4.5. Nonlinear Segmentation Algorithm for Lung CT

The hierarchical segmentation procedure is as follows:

- Calculate the TV flow evolution for the CT at different scales in Equation 9:

$$L^{(k+1)} = L^{(k)} + \Delta t div\left(\frac{\nabla L^{(k)}}{|\nabla L^{(k)}|}\right) \quad (9)$$

- At each scale k, the image is partitioned into connected components of isolevel sets.
- Use connections to link areas at various levels:
  - Overlap between regions
  - Minimal gray-level distance
- Stop at a chosen scale Sstop that indicates the level of granularity of the segmented nodules and fibrosis.
- Bring together all the regions that are connected to the same node at Sstop to form final segmented objects.

Figure 15 provides a visualization of our processing pipeline for HRCT lung images. The scale-space stack and segmentation of an exemplary CT slice is illustrated in Figure 16. 16(a) shows the original CT slice; 16(b), 16(d), and 16(f) show the TV-flow results at different scales, while 16(c), 16(e), and 16(g) show the matching segmented nodules and fibrotic areas.

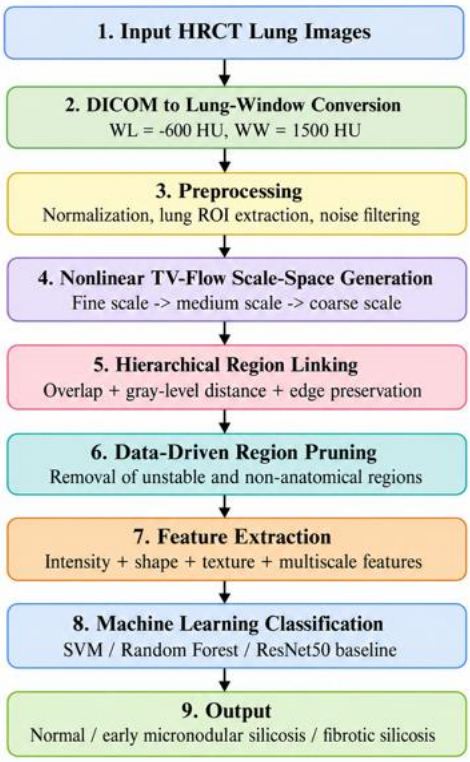

Figure 15. Proposed methodology for silicosis detection using HRCT data

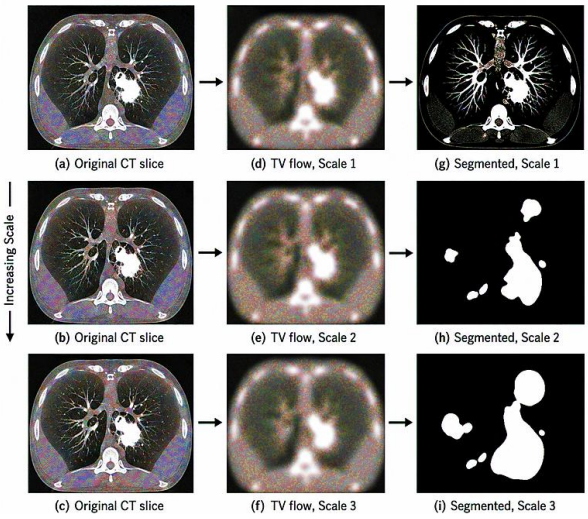

Figure 16. Scale-space stack and segmentation of a lung CT slice: (a) original CT slice, (b,d,f) TV flows at different scales, (c,e,g) segmented nodules and fibrosis.

4.6. ML-based enhanced silicosis detection

A set of appropriate features is extracted from each region of interest (ROI) to describe the normal and abnormal lung parenchyma. The mean and standard deviation of the intensity of the gray-level values are among the intensity features. Several shape features (such as area, perimeter, eccentricity and compactness) are used to describe the shape of nodules and FPs after we apply Scale-Invariant Feature Transform (SIFT)-based key point descriptor. Texture features (eg GLCM descriptors, LBP and wavelet coefficients) represent spatial distribution of intensity and heterogeneity of tissue type. Multiscale features based on the scale-space representation additionally enable the discrimination of lesions at different scale. These features are then fed into machine-learning classifiers such as the Random Forest and the Support Vector Machines to detect silicosis.

ML-Based Silicosis Detection Detection Each connected segmented lung region is mode led using four feature groups (described next) for ML-based silicosis detection. The mean, standard deviation, minimum and maximum (four intensity features) are used to describe the gray level variation in HRCT images. Geometrical ones – these give you an idea of how big the lesion was and how it looked (its shape). Texture features, such as LBP and GLCM contrast, correlation and entropy, are used to differentiate nodular, fibrotic and heterogeneous tissue patterns. Multiscale features such as hierarchy depth and scale-dependent variance provide clues for identifying lesions at different sizes and image scales [2, 6, 7].

Figure 17 provides a summary of the extracted features. The feature vector contains intensity features(mn, std, min, and max), shape features(area, perimeter, eccen, and round) texture features (GLCM contrast, correlation, entropy and LBP), and multiscale features(hierarchy depth and scale-dependent var). The TV-flow segmentation and machine-learning scheme yields a Dice score of 0.91, a precision of 0.92, a recall of 0.89, an accuracy of 0.94, and an F1-score of 0.90, indicating the potential of the proposed framework for silicosis detection.

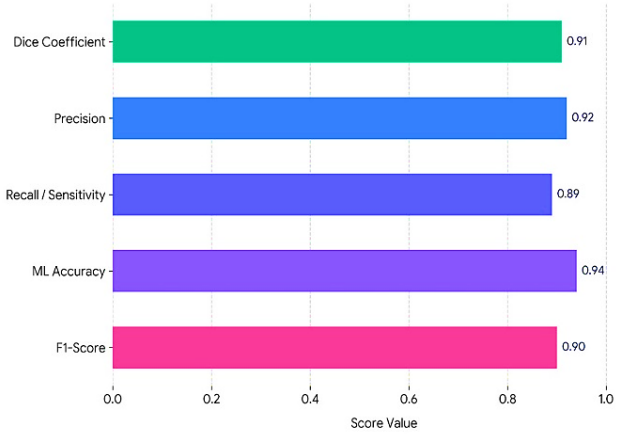

Figure 17. Lung region features extracted for ML-based silicosis detection

Cases of occupational silicosis were assessed with axial high-resolution computed tomography (HRCT) of the chest. The DICOM images were transformed to gray-scale lung-window images with a window center of −600 HU and a window width of 1500 HU. The dataset consisted of normal lung parenchyma, early micronodular silicosis and late fibrotic silicosis. Radiologist-administered lesion masks were employed as the ground truth for the calculation of Dice score, precision, and recall. Patient wise splitting was employed to avoid leakage between slices, 70% subjects were used for training, 15% for validation, and 15% for testing.

The nonlinear TV-flow scale-space segmentation and the feature-based machine-learning classification strategy exploiting a local-global approach within a scale-space analysis in the proposed framework are novel and very powerful tool for silicosis proposed in this article by discriminating nodular and fibrotic abnormalities from normal lung.

5. EXPERIMENTAL RESULTS

5.1 Dataset Description and Experimental Protocol

The dataset consisted of 64 subjects and 286 axial HRCT slices with a matrix of 512 × 512 pixels. Subjects were divided into three diagnostic groups: 22 normal/control subjects, 21 patients with early micronodular silicosis, and 21 with fibrotic silicosis. The cohort was shared by participants with a mean 52.8 ± 9.7 years of age, 58 male and 6 female participants; (exposed subjects only) mean documented duration of occupational silica-exposure was 16.4 ± 6.2 years.

Radiologist -estimated nodular and fibrotic lesion masks served as reference annotations for the supervised feature extraction and validation of the segmentation. Subject-wise rather than slice-wise partitioning was applied to avoid information leakage: 44 subjects (70%) were used for training, 10 (15%) for validation, and 10 (15%) for testing. Inclusion criteria were age ≥18 years, availability of an axial HRCT of diagnostic quality, categorization in a normal/control or silicosis group, and reviewable radiological annotations, and for silicosis cases, documented occupational silica exposure. Exclusion criteria were severe artifacts on imaging, incomplete/duplicate studies, missing annotations, major thoracic surgery or comorbid pulmonary disease that interfered with precise silicosis annotation.

5.2. Performance of the Multiscale Segmentation Algorithm with Edge Preservation

The multiscale image-segmentation method was tested on lung CT images for silicosis detection. Under TV-flow evolution, Figure 18(a) is the original image and figures 18(b) to 18(d) represent flow evolution, segmentation and contour extraction at three increasingly coarser scales.

Fine scales keep small nodules and early fibrotic lesions that enable detection of subtle pathological changes as shown in Figure 18(b) and (c). At medium scales, discrete nodules coalesce into extensive fibrotic regions, and local parenchymal texture perturbations are diffused. At coarse scales the largest masses of fibrosis and lung regions emerge and are helpful in analyzing pattern of advanced disease.

Only one implicit parameter, the scale parameter S, determines how coarse or fine the segmentation is. In all the simulations, the time step Δt=0.025 in TV flow was fixed.

5.3. Robustness to Noise

To simulate low-doselike CT degradation, zero-mean Gaussian noise was added synthetically to the original HRCT slices. For this reason, Figure 19 shows simulated noisy images and not scans from a separate low-dose CT dataset. The proposed algorithm kept small nodules and fibrotic regions in the presence of simulated degradation.Figure 19(a) is the noisy CT image, Figure 19(b) is the TV-flow result at S = 2048, Figure 19(c) shows the segmented nodular and fibrotic areas, and Figure 19(d) displays the segmentation contours on top of the noisy input image.

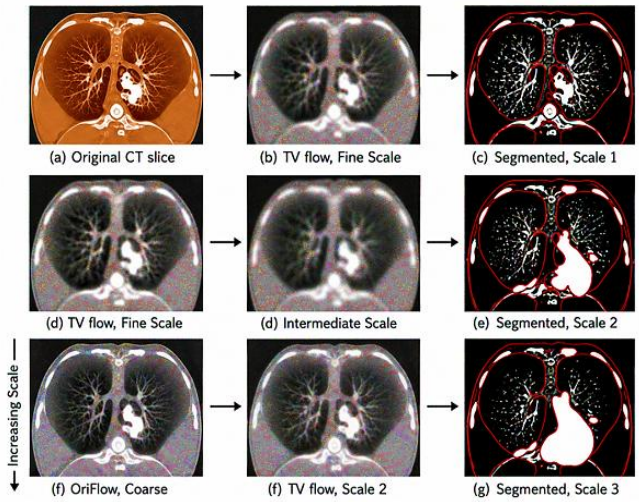

Figure 18. Multiscale segmentation of lung CT slice using TV flow. (a) Original CT; (b,d,f) TV flow evolution at increasing scales; (c,e,g) segmented regions; (h,j,l) contours of segmented objects.

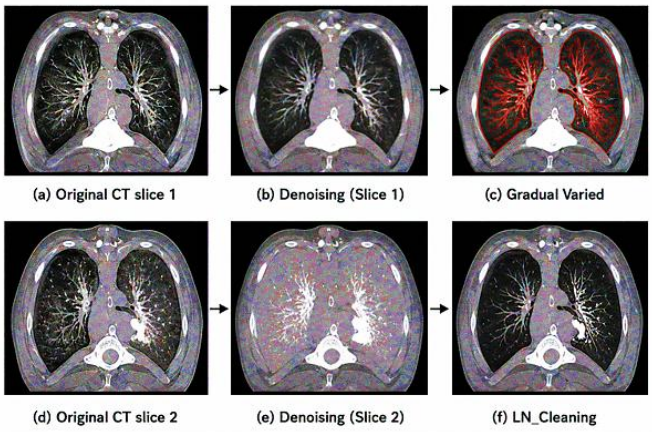

Figure 19. Robust segmentation in simulated noisy CT conditions. The HRCT slice of the clean CT image has been synthetically corrupted with Gaussian noise at PSNR = 25 dB: (a) CT image with added Gaussian noise, (b) TV-flow output (S = 2048), (c) segmented nodules/fibrotic regions, (d) contour overlay.

Zero-mean Gaussian noise was implemented for noise simulation as in Equation 10:

$$I_{noisy} = \mathrm{I} + \mathrm{n}, \text{where } \mathrm{n} \sim \mathrm{N}(0, \sigma^2) \qquad (10)$$

The intensities of all the CT images were rescaled to [0, 1]. The noise standard deviation, estimate, was calculated from the target psnr using Equation 11.

$$\sigma = \sqrt{(10^{(-PSNR/10)})} \qquad (11)$$

The robustness test was also conducted at the PSNR levels of 30, 25, 20, and 15 dB, and the result is illustrated in Figure 20. These parameters simulate increasingly severe noise conditions, from light to heavy distortion.

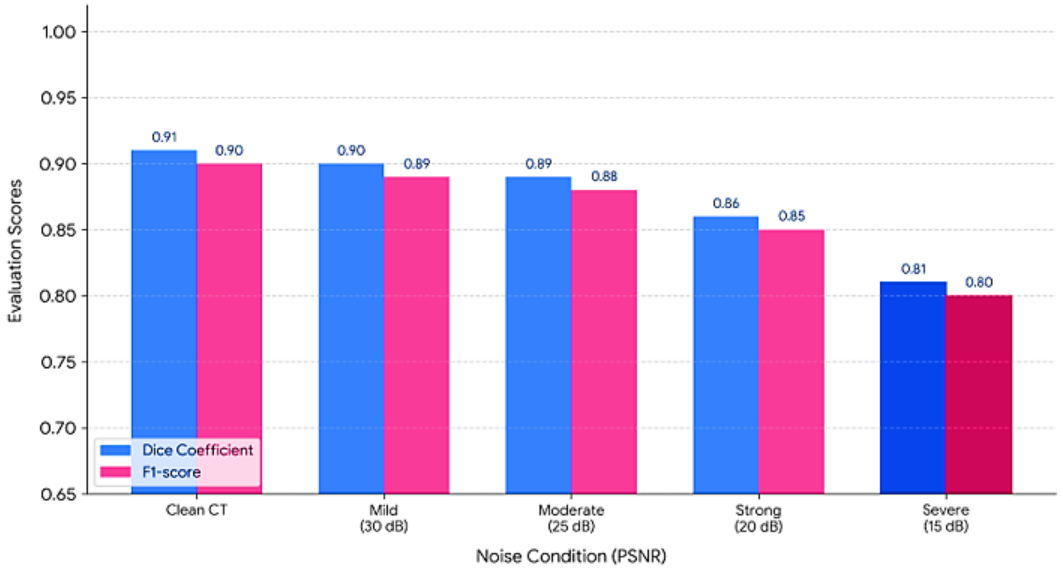

Figure 20. Robustness Evaluation Under Different Gaussian Noise Levels

Results indicate that the proposed TV-flow segmentation is not affected by moderate and mild noise. The method is less affected by severe noise conditions than thresholding and watershed segmentation, and retains more of the large-scale fibrotic boundaries.

5.4. Comparison with Other Segmentation Methods

We compared our method with the conventional and representative state-of-the-art lung CT image segmentation methods. Figure 21 depicts the comparison in terms of edge preservation, region consistency, and scale behavior. Figure 22 displays classical results, such as intensity thresholding, maximum-likelihood clustering and gradient watershed segmentation. Figure 23 displays active-contour methods: the geodesic and Mumford-Shah models. Figure 24 shows the proposed multiscale TV-flow segmentation at fine, intermediate and coarse scales.

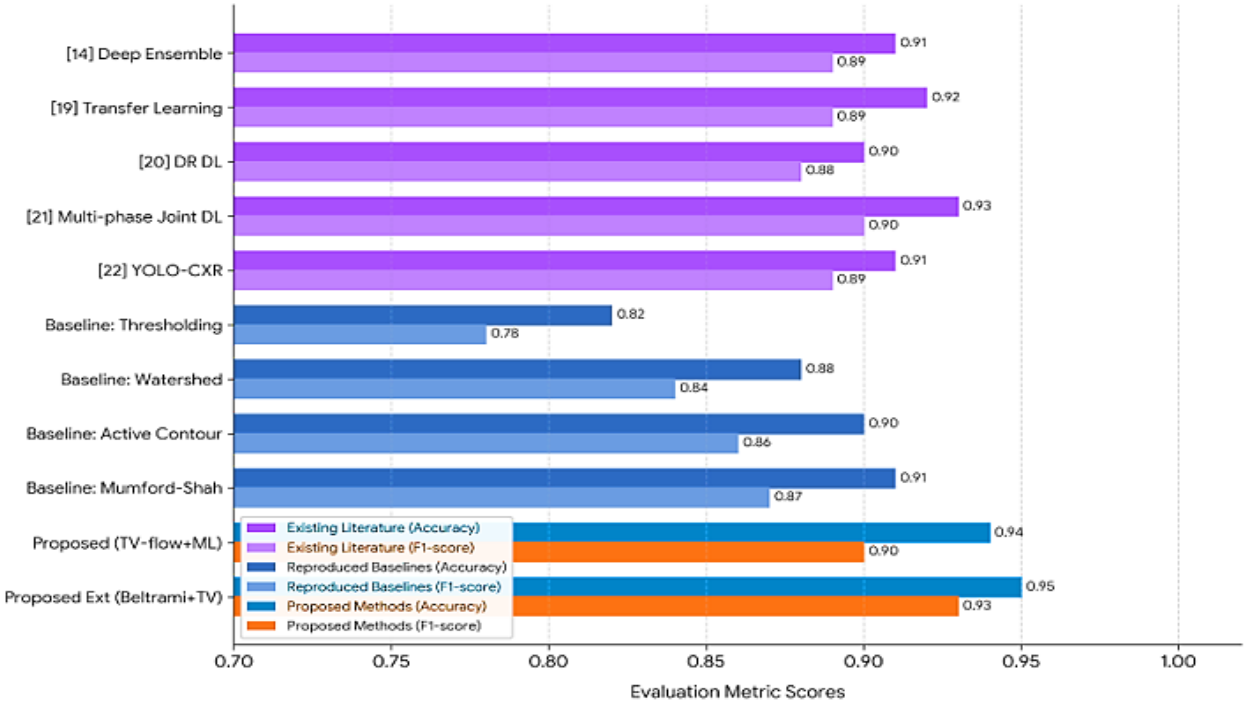

Figure 21. Comparing the proposed method with the existing segmentation and AI-based methods

Comparison indicates that deep-learning based methods achieve strong results at the image level, but they typically do not explicitly segment lesions in the CT. Classical segmentation methods yield interpretable regions, but they may be sensitive to noise, intensity variation, and initialization. In contrast, the TV-flow

multiscale framework is able to preserve lesion boundaries, generate region-level features, and deliver uniform segmentation performance which leads to the best Dice score and classification accuracy.

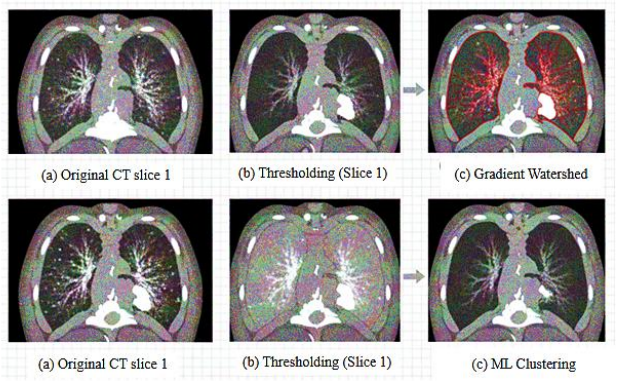

Figure 22. Classical segmentation on lung CT: thresholding, ML, gradient watershed.

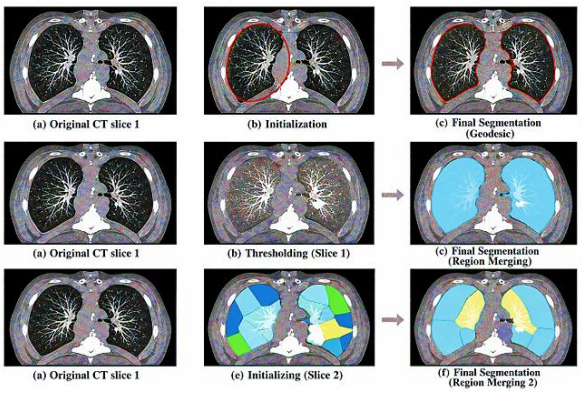

Figure 23. Active contour segmentation: geodesic and Mumford-Shah models.

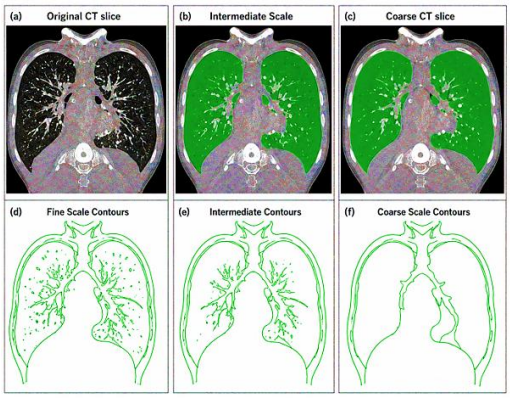

Figure 24. Multiscale TV flow segmentation on lung CT: fine, intermediate, coarse scales.

5.5. Effect of Scale Parameter on Silicosis Segmentation

The scale at which we stop, S, influences the amount and size of the nodular and fibrotic regions that are found. The segmentation results at various scales are presented in Figure 25. Upper row: segmented regions; lower row: contours of the segmented regions on the original CT slice. Stopping scales are (a) S = 2048, (b) S = 24,576, (c) S = 49,152, and (d) S = 131,072. Table 2 displays the associated number of segment regions.

Table 2. The results from segmentation across the different scales of stopping.

Scale (S)	# Regions Segmented
2048	38
24576	22
49152	10
131072	4

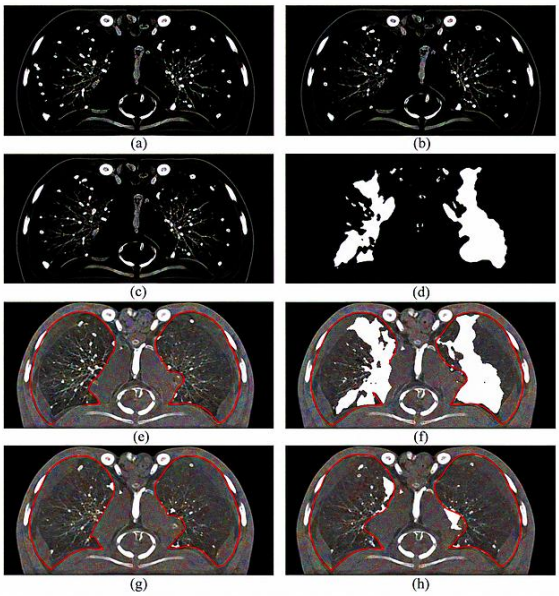

Figure 25. Segmentation results for different scale levels. Top row: segmented regions; bottom row: contours overlaid on original CT. (a) S=2048S = 2048S=2048; (b) S=24576S = 24576S=24576; (c) S=49152S = 49152S=49152; (d) S=131072S = 131072S=131072.

5.6. Feature Extraction and Machine Learning Integration

Features from each segmented region are extracted and fed to a ML classifier. Intensity-based features of mean, standard deviation, minimum and maximum pixel intensities were used to describe CT-density variation. Shape features (area, perimeter, eccentricity, solidity) denote the geometry of the lesion. Textural features such as GLCM contrast, correlation, energy, LBP, nodular and fibrillar patterns are motion invariant. Scale-space depth and scale variance were combined to detect scale-varying abnormalities.

These features were then fed into the silicosis diagnosis Random Forest and SVM classifiers. The accuracy of the TV-flow segmentation and ML classification scheme is given in Table 3. The segmentation module was able to reach a dice score of 0.91, precision of 0.92 and recall of 0.89.

Table 3. ML classification performance

Metric	Value (TV Flow + ML)
Dice coefficient	0.91
Precision	0.92
Recall	0.89
Accuracy	0.94
F1-score	0.90

The fine-scale segmentation facilitates the detection of small nodules typical of the early disease, while the coarser-scale representations address the integration of major fibrotic areas.

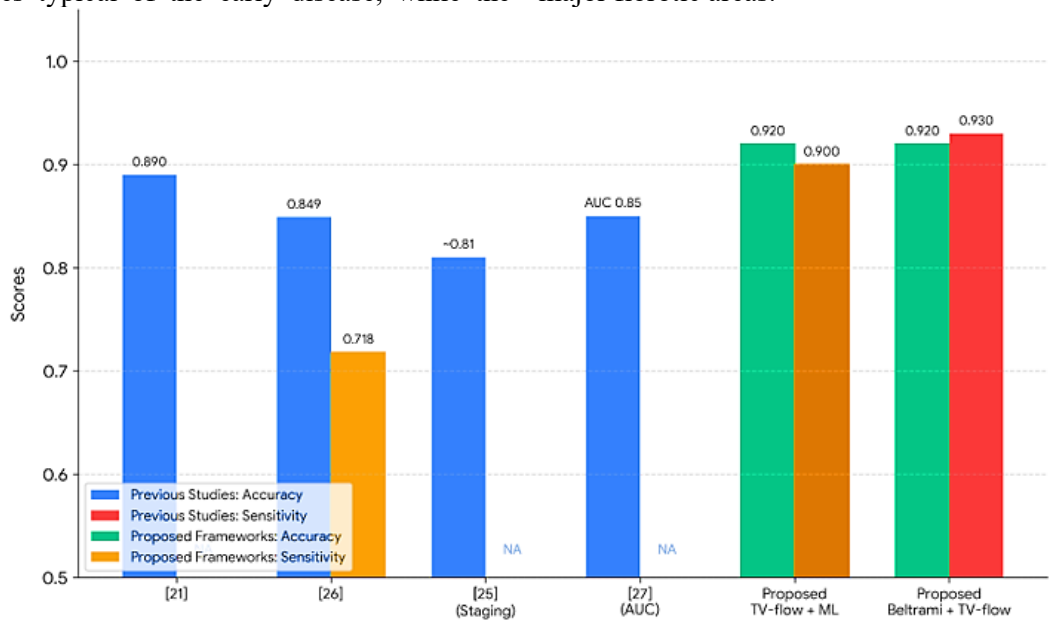

Figure 26. Comparison of classification performance with previous studies.

As can be seen in Figure 26, our proposed method gained the accuracy of 94% and F1-score of 0.90 with the HRCT region-level features. In contrast to prior work largely focused on image-level deep learning with chest radiographs, our method results in interpretable CT lesion segmentation prior to classification. This allows for not only disease classification but also the identification of locations of micronodules and fibrotic areas.

5.7. The study of Deep Learning Baseline and GAN-Augmentation.

Similarly, further experiments were carried out to evaluate our proposed region based ML framework against popular AI baselines, e.g., ResNet50 transfer learning, and GAN based data augmentation. ResNet50 was pretrained on ImageNet weights, and then fine-tuned on lung-window CT images and lung ROIs. GAN augmentation was applied to increase the number of lesion samples, with visual inspection to reduce the introduction of unrealistic synthetic lesion patterns, as summarized in Figure 27.

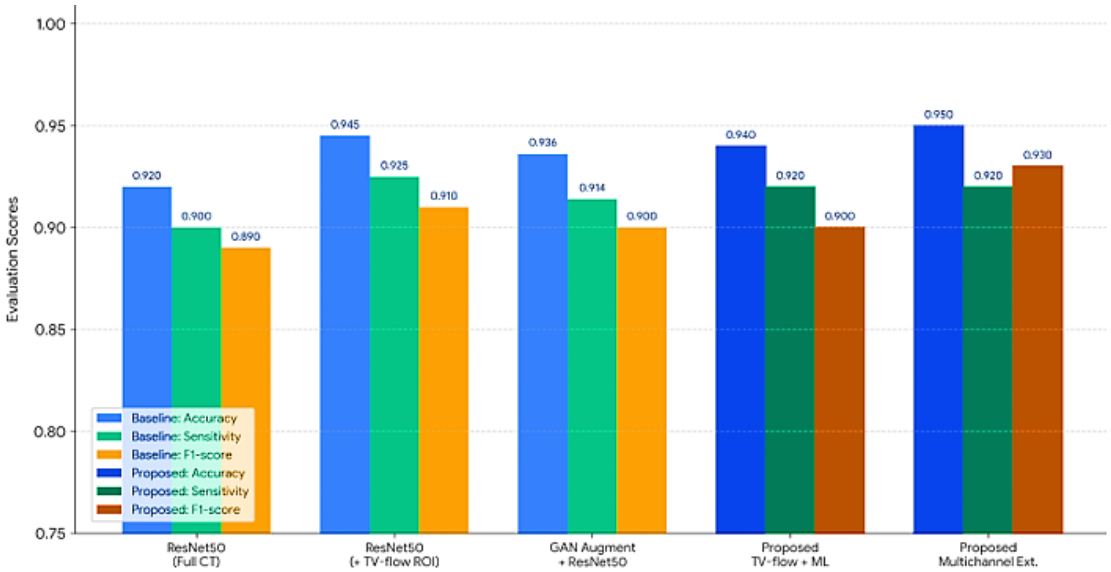

Figure 27. A comparison of the performance of the proposed methods and the deep learning baselines.

5.8. Computational Complexity and Processing Time

Complexity analysis was performed for the TV-flow segmentation, hierarchical region linking, feature extraction, and Random Forest classification on CPU-based. Let N be the number of pixels in a CT slice, K the number of TV-flow iterations/scale updates, R the number of retained segmented regions, d the number of features extracted per region, T the number of trees in the Random Forest and D the average depth of a tree. The cost of dominant segmentation and linking is given

by Equation 12, that of feature extraction by Equation 13, and of classification by Equation 14. The total end-to-end complexity is thus summarized in Equation 15.

$$T_{seg}(N,K,R) = O(KN + KR\,log\,R) .. \quad (12)$$

$$T_{feat}(N,R,d) = O(N + Rd) \quad (13)$$

$$T_{RF}(R,T,D) = O(RTD) \quad (14)$$

$$T_{total} = T_{seg} + T_{feat} + T_{RF} \quad (15)$$

In Equations 12–15. N = 512 × 512 pixels for each HRCT slice; K is specified by the chosen flow evolution schedule in TV-flow; R depends on the stopping scale; d is the region-feature dimension; T is the number of Random Forest trees; The average depth of the tree is denoted with D. The memory usage is in the order of magnitude of O(N + Rd) for the per-region pipeline (except for holding the DICOM volume).

Processing time was monitored per 512 × 512 slice with a tentative implementation environment of Windows 11 (64bit), an Intel Core i7-12700H, 16 GB RAM, Python 3.11 by CPU for the TV-flow/feature/Random Forest pipeline. Results were averaged over multiple runs post-initialization. As shown in Table 4, the average processing time for the entire procedure was ~1.22 ± 0.15 s per slice, with the most runtime-consuming steps being segmentation and hierarchical linking.

Table 4. Complexity of computation and average processing time per 512 × 512 HRCT slice.

Pipeline stage	Complexity	Mean time (s)
Preprocessing/windowing	O(N)	0.07 ± 0.01
TV-flow + hierarchical linking	O(KN + K R log R)	0.94 ± 0.13
Feature extraction	O(N + R d)	0.19 ± 0.03
Random Forest classification	O(RTD)	0.02 ± 0.01
End-to-end pipeline	Equation 15	1.22 ± 0.15

Table 4 shows that the proposed workflow fits well into offline or near-interactive CAD analysis on the commodity workstation hardware, albeit full-volume clinical deployment will require optimized parallel execution. The timing results do not demonstrate real-time clinical performance and should be validated prospectively with the final implementation and typical clinical CT volumes.

6. EXTENSION TO MULTICHANNEL (COLOR AND PSEUDO-COLOR) IMAGES FOR SILICOSIS DETECTION

Chest CT and X-rays are usually grayscale, though multichannel representations are being more frequently used in medical-image analysis (e.g., pseudo coloring of CT maps, RGB overlays of multiscale information, or individual channels of multi-energy CT). Our nonlinear multiscale segmentation framework can be extended to such vector-valued images and is expected to enhance characterization of silicosis patterns.

6.1. Edge-Preserving Nonlinear Diffusion for Multichannel Lung Images

To broaden the scope of the framework to color or multichannel images, a diffusion model that is edge preserving uniformly over all channels is necessary. In this paper, we employ the Beltrami flow for vector-valued images [13] as a natural multichannel extension of the TV-based diffusion framework of Equation 16 discussed previously.

Let $I(x,y) = [I_1(x,y),\ I_2(x,y), \ldots . I_n(x,y)]$ (16)

I(x,y) is a multichannel image of the lungs (e.g., RGB pseudo-color CT, fused feature maps. The Beltrami flow evolves the image according to the Equation 17.

$$\frac{\partial I}{\partial t} = div\,\frac{\nabla I}{1+\|\nabla I\|^2} \quad (17)$$

This is how the homogeneous regions of the lungs are smoothed without perturbing the boundaries of the nodules and fibrotic areas. It also avoids the edge misalignment problem, and preserves consistency on the channels, or feature maps. Pseudo-color lung CT image is diffused to different channels via Beltrami flow as seen in Figure 28.

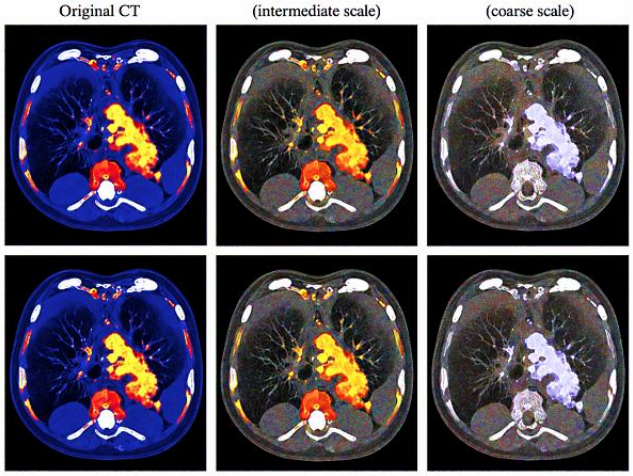

Figure 28. Multichannel diffusion of lung CT pseudo-color image using Beltrami flow at increasing scales.

6.2. Region Partitioning Using Perceptually Meaningful Color Metrics

After multiscale diffusion, the image is divided into segments where each segment corresponds to a group of similar anatomical or pathological structures. This calls for a notion of color or channel similarity. A naive method is applying Euclidean distance in RGB space according to the Equation 18.

$$d_{RGB} = \sqrt{(\nabla R)^2 + (\nabla G)^2 + (\nabla B)^2} \quad (18)$$

However, the RGB space is not perceptually uniform so equal numerical differences in color values may not correspond to equal visual differences. This constraint

is important also when looking for small changes in lung-tissue patterns.

To overcome this issue we use the CIELUV colour space, which is perceptually uniform. The difference in colours is computed as shown in Equation (19).

$$d_{CIELUV} = \sqrt{(\nabla L^*)^2 + (\nabla u^*)^2 + (\nabla v^*)^2} \quad (19)$$

Application of CIELUV enhances discrimination between fibrotic patterns and normal parenchyma, facilitating identification of abnormal areas and yielding more stable grouping of pseudo-colored CT areas. In the the studied lung images, RGB exhibited the least perceptual uniformity and edge preservation, HSV had a moderate performance, and CIELUV was the best both in terms of color uniformity and edge-preservation, thus it was considered the best representation for analyzing silicotic lung-regions.

6.3. Hierarchical Linking Across Scales in Multichannel Images

After splitting the multichannel images into connected components of isolevel sets, we construct a hierarchical tree by connecting regions between consecutive scales, in the same manner as above.

For multichannel images, the perceptual color difference is computed in the CIELUV color space instead of in the one dimensional grayscale space. Regions are connected if and only if they have a spatial intersection. Among the ambiguous regions of overlap, the parent is chosen by the minimum perceptual color distance, which ensures better color consistency at different scales.

Beltrami flow maintains strong edges at multiscales and attenuates false connections between lung parenchyma, nodules, and fibrotic regions. Figure 29 shows hierarchical region matching at different scales, where the matching (child) regions at smaller scales are linked to their matching (parent) regions at larger scales.

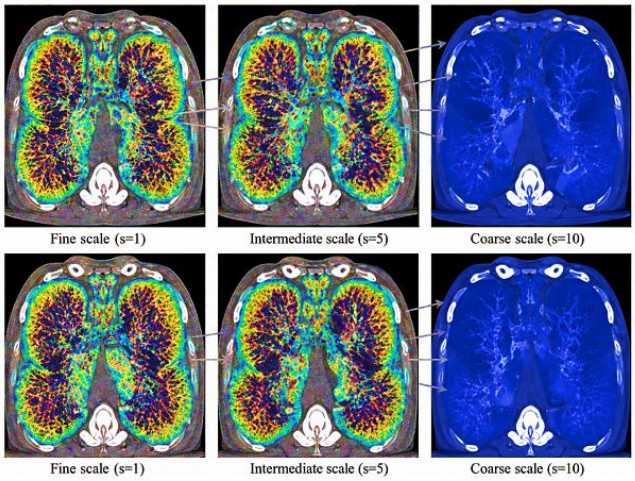

Figure 29. Hierarchical multiscale linking of multichannel lung regions.

6.4. Segmentation Results on Lung Images in Pseudo-Color

The result of segmenting a pseudo-color lung CT image at different stopping scales S is shown in Fig. 30 Fine scales preserve individual small silicosis nodules and local texture, middle scales group single nodules to larger fibroid lesions, and large scales emphasize the largest pathological areas.

The multilevel adaptive decomposition enables a clinician, or machine learning algorithm, to select the scale of segmentation suitable for the application of interest. Here (Figure 30), the top panel displays the segmentation results, and the bottom panel shows the associated contours superimposed on the original image.

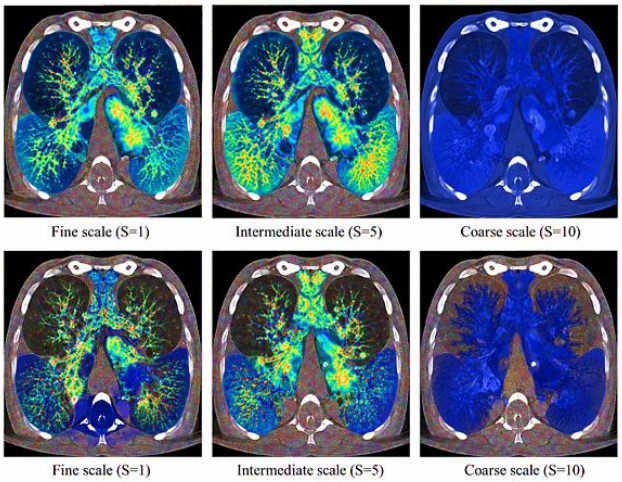

Figure 30. Pseudo-color lung image segmentation at different stopping scales.

6.5. Benefits for Machine Learning-Based Silicosis Detection

For machine-learning analysis, multichannel segmentation – by fusing channel-dependent statistics with multiscale structural information – allows more fine-feature representation. This representation is more invariant to noise and intensity variation and has better performance in separating overlapped pathological distributions. Since there is anatomical or pathological meaning to the segmented regions, more discriminative region-level features can be used by the classifier.

The effect of the multichannel segmentation on the ML results is summarized in Figure 31. Accuracy, F1-score and recall without scale-space processing were 0.86, 0.84 and 0.82, respectively. Grayscale TV-flow processing merged these values up to 0.91, 0.90 and 0.89. The multichannel Beltrami diffusion further improved the accuracy to 0.95, the F1-score to 0.93 and the recall to 0.92, indicating the superiority of multichannel multiscale (mms) segmentation for silicosis detection.

6.6. Discussion

The multichannel generalization allows us to apply the proposed framework to clinically relevant medical-image representations. Relevant open issues are the best choice of color space and diffusion parameters. Nonetheless, the results suggest that edge-preserving multichannel nonlinear scale space segmentation is a suitable preprocessing for machine learning based silicosis detection.

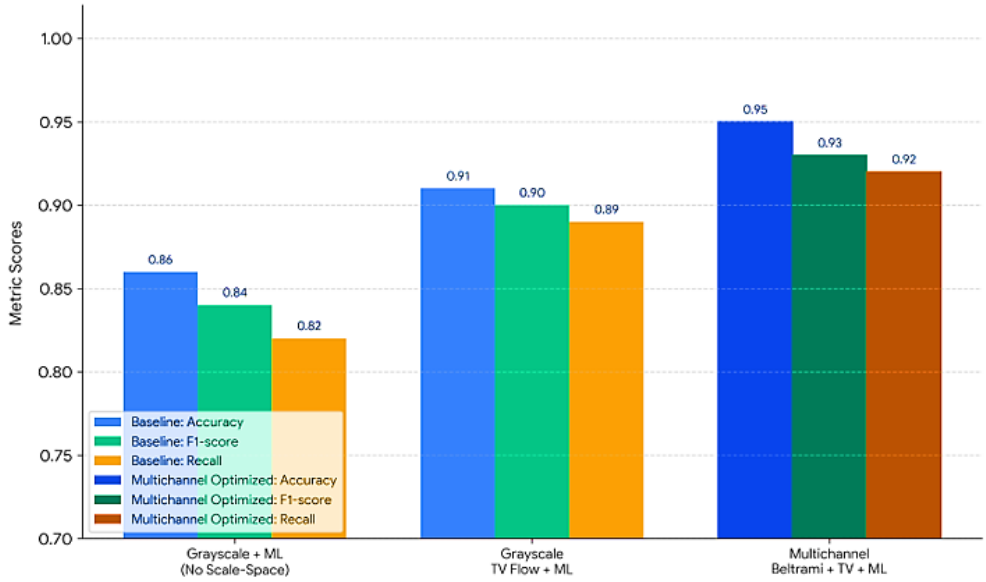

Figure 31. The effect of multichannel segmentation on the performance of ML

7. DISCUSSION AND CLINICAL IMPLICATIONS

The results of the experiment indication: enable the proposed multiscale nonlinear scale-space framework to be a promising tool for the segmentation of silicosis related lung abnormalities, especially when TV and Beltrami flows are employed. This part discusses the methodological strengths, the clinical importance, the limitations, and the needs for future clinical application.

7.1. Advantages of Multiscale Nonlinear Segmentation for Silicosis

Silicosis results is pathological patterns at multiple spatial scales. Early disease may be in the form of small nodules, while late disease may show widespread fibrosis. Single-scale segmentation approaches thus may fail to extract small lesions or connect abnormal tissues with normal lungs.

In order to overcome this problem, the proposed nonlinear multiscale approach preserves the multiscale edges and patterns. It enables a progressive simplification of the lung structure. A similar method can also be used to generate a hierarchical view of the lungs ranging from fine to coarser information.

Unlike thresholding, clustering or watershed segmentation, our approach does not make one single fixed assumption on intensity or size of the object. Instead pathological regions are produced in a scale-space evolution by hierarchical linking thereby providing a structured representation across lesion sizes.

7.2. Role of Edge Preservation in Clinical Reliability

Edge preservation is a fundamental necessity in the segmentation of medical images, especially in lung disease with weak nodule and fibrosis boundaries. TV flow and Beltrami flow smooth homogeneous tissue while preserving major boundaries. This prevents abnormal and normal regions from being merged inappropriately, also helps retain early-stage nodules during denoising, and reduces false boundaries introduced by noise of image or variation of texture.

The resulting better edge preservation may thus enable more robust automated segmentation, as well as provide regions that are easier to be inspected by clinicians or analyzed by downstream classifiers.

7.3. Discussion of Implications for Machine Learning-Based Diagnosis

One major implication of this work is the introduction of region-level information for machine-learning diagnosis. Training classifiers on segmented regions instead of all image pixels directly enhances the meaningfulness of shape, texture, and multiscale features related to well-defined lung structures. It also eliminates some of the redundancy of pixel level information while still allowing classifiers to be applied at different segmentation scales. These features might allow better sensitivity for detecting both early micronodular disease and end-stage fibrotic disease.

7.4. Clinical Workflow Integration

In this sense, the suggested pipeline can be used in a CAD system in a decision support perspective instead of being an independent diagnostic system. Multiscale segmentations, regions of interest, and interpretable region-level features can be automatically extracted from standard HRCT images. A radiologist could then examine the outlined areas at a scale considered appropriate in clinical practice for screening, monitoring disease progression, or estimating severity. The system, however, would need prospective validation, integration into DICOM/PACS workflows, and multi-scanner, reconstruction protocol, and patient population testing prior to clinical application.

7.5. Generalization and Modality Independence

Although this work is developed in the context of silicosis, the multiscale framework is not the any specific disease. Since nonlinear scale-space techniques have been used on noisy and medical images [9], the method can also be explored for other occupational lung

diseases such as asbestosis and coal workers' pneumoconiosis, and for interstitial lung diseases. However, such generalization should be proven by disease-specific external validation.

7.6. Limitations and Future Directions

Several considerations should be kept in mind. First, the sample size is small (64 subjects and 286 HRCT slices), which limits the statistical precision of the performance estimates presented and may potentially allow overfitting. Second, there is also no independent external or multicenter test cohort, and thus the scanner, reconstruction, demographic, and disease-prevalence variations in real-world practice have not been quantified.

Future research will incorporate larger and more heterogeneous populations, external and prospective validation, blinded multi-radiologist comparison, decision threshold calibration to minimize clinically relevant false positives and false negatives, and investigation of workflow effects.

7.7. Clinical Significance

The multiscale nonlinear segmentation offers interpretable region extraction, edge stability, and lesion localization to facilitate future computer-aided silicosis evaluation. Its role in the clinical setting is to help the radiologist raise the attention toward potentially suspicious micronodular and fibrotic areas and not to substitute the human expert in the interpretation. Thus, the system requires the radiologist's validation on a higher number of cases before proving its applicability in the routine screening, diagnosis and monitoring.

8. CONCLUSION

The nonlinear multiscale segmentation scheme enhances analysis of silicosis-related lesions in lung scans by integrating edge-preserving PDE diffusion (TV flow and Beltrami flow), hierarchical region merging and region-level machine-learning classification. The proposed method obtained Dice=0.91, precision=0.92, recall=0.89, overall classification accuracy=0.94 and F1-score=0.90. Region-based feature extraction condensed redundant information and resulted in meaningful localization of micronodules and fibrotic regions. The framework is insensitive to simulated low-dose-like noise and can be applied to multichannel pseudo-color images, with a best experimental accuracy of 0.95. However, the relatively small data set and lack of external prospective validation preclude direct clinical generalization.

REFERENCES

[1] R. F. Hoy, M. F. Jeebhay, C. Cavalin, W. Chen, R. A. Cohen, E. Fireman, L. H. T. Go, A. León-Jiménez, A. Menéndez-Navarro, M. Ribeiro, and P.-A. Rosental, "Current global perspectives on silicosis—Convergence of old and newly emergent hazards," *Respirology*, vol. 27, no. 6, pp. 387–398, 2022, doi: 10.1111/resp.14242.

[2] A. León-Jiménez, J. M. Mánuel, M. García-Rojo, M. G. Pintado-Herrera, J. A. López-López, A. Hidalgo-Molina, R. García, P. Muriel-Cueto, N. Maira-González, D. Del Castillo-Otero, and F. M. Morales, "Compositional and structural analysis of engineered stones and inorganic particles in silicotic nodules of exposed workers," *Part. Fibre Toxicol.*, vol. 18, Art. no. 41, 2021, doi: 10.1186/s12989-021-00434-x.

[3] A. León-Jiménez, A. Hidalgo-Molina, M. Á. Conde-Sánchez, A. Pérez-Alonso, J. M. Morales-Morales, E. M. García-Gámez, and J. A. Córdoba-Doña, "Artificial stone silicosis: Rapid progression following exposure cessation," *Chest*, vol. 158, no. 3, pp. 1060–1068, 2020, doi: 10.1016/j.chest.2020.03.026.

[4] A. García-Núñez, G. Jiménez-Gómez, A. Hidalgo-Molina, J. A. Córdoba-Doña, A. León-Jiménez, and A. Campos-Caro, "Inflammatory indices obtained from routine blood tests show an inflammatory state associated with disease progression in engineered stone silicosis patients," *Sci. Rep.*, vol. 12, no. 1, Art. no. 8211, 2022, doi: 10.1038/s41598-022-11926-x.

[5] W. Sun, D. Wu, Y. Luo, L. Liu, H. Zhang, S. Wu, Y. Zhang, C. Wang, H. Zheng, J. Shen, and C. Luo, "A fully deep learning paradigm for pneumoconiosis staging on chest radiographs," *IEEE J. Biomed. Health Inform.*, vol. 26, no. 10, pp. 5154–5164, 2022, doi: 10.1109/JBHI.2022.3190923.

[6] L. Zhang, R. Rong, Q. Li, D. M. Yang, B. Yao, D. Luo, X. Zhang, X. Zhu, J. Luo, Y. Liu, X. Yang, X. Ji, Z. Liu, Y. Xie, Y. Sha, Z. Li, and G. Xiao, "A deep learning-based model for screening and staging pneumoconiosis," *Sci. Rep.*, vol. 11, no. 1, Art. no. 2201, 2021, doi: 10.1038/s41598-020-77924-z.

[7] F. Yang, Z.-R. Tang, J. Chen, M. Tang, S. Wang, W. Qi, C. Yao, Y. Yu, Y. Guo, and Z. Yu, "Pneumoconiosis computer aided diagnosis system based on X-rays and deep learning," *BMC Med. Imaging*, vol. 21, no. 1, Art. no. 189, 2021, doi: 10.1186/s12880-021-00723-z.

[8] F. Mushtaq, S. Bhattacharjee, S. Mandia, K. Singh, S. S. Chouhan, R. Kumar, and P. Harjule, "Artificial intelligence for computer aided detection of pneumoconiosis: A succinct review since 1974," *Eng. Appl. Artif. Intell.*, vol. 133, Art. no. 108516, 2024, doi: 10.1016/j.engappai.2024.108516.

[9] M. Mirbabaie, S. Stieglitz, and N. R. J. Frick, "Artificial intelligence in disease diagnostics: A critical review and classification on the current state of research guiding future direction," *Health Technol.*, vol. 11, no. 4, pp. 693–731, 2021, doi: 10.1007/s12553-021-00555-5.

[10] L. Devnath, S. Luo, P. Summons, and D. Wang, "Automated detection of pneumoconiosis with multilevel deep features learned from chest X-ray radiographs," *Comput. Biol. Med.*, vol. 129, Art. no. 104125, 2021, doi: 10.1016/j.compbiomed.2020.104125.

[11] D. Sanchez-Morillo, A. León-Jiménez, M. Guerrero-Chanivet, G. Jiménez-Gómez, A. Hidalgo-Molina, and A. Campos-Caro, "Integrating routine blood biomarkers and artificial intelligence for supporting diagnosis of silicosis in engineered stone workers," *Bioeng. Transl. Med.*, vol. 9, no. 6, Art. no. e10694, 2024, doi: 10.1002/btm2.10694.

[12] X. Xue, D. Ji, C. Xu, Y. Zhao, Y. Li, and C. Hu, "Adaptive orthogonal directional total variation with kernel regression for CT image denoising," *J. X-Ray Sci. Technol.*, vol. 32, no. 5, pp. 1253–1271, 2024, doi: 10.3233/XST-230416.

[13] Z. Mustafa and H. Nsour, "Using computer vision techniques to automatically detect abnormalities in chest X-rays," *Diagnostics*, vol. 13, no. 18, Art. no. 2979, 2023, doi: 10.3390/diagnostics13182979.

[14] L. Devnath, S. Luo, P. Summons, D. Wang, K. Shaukat, I. A. Hameed, and F. S. Alrayes, "Deep ensemble learning for the automatic detection of pneumoconiosis in coal worker's chest X-ray radiography," *J. Clin. Med.*, vol. 11, no. 18, Art. no. 5342, 2022, doi: 10.3390/jcm11185342.

[15] A. Davri, E. Birbas, T. Kanavos, G. Ntritsos, N. Giannakeas, A. T. Tzallas, and A. Batistatou, "Deep learning for lung cancer diagnosis, prognosis and prediction using histological and cytological images: A systematic review," *Cancers*, vol. 15, no. 15, Art. no. 3981, 2023, doi: 10.3390/cancers15153981.

[16] M. A. Balcı, L. M. Batrancea, Ö. Akgüller, and A. Nichita, "A series-based deep learning approach to lung nodule image classification," *Cancers*, vol. 15, no. 3, Art. no. 843, 2023, doi: 10.3390/cancers15030843.

[17] Y. H. Bhosale and K. S. Patnaik, "Application of deep learning techniques in diagnosis of COVID-19 (Coronavirus): A systematic review," *Neural Process. Lett.*, vol. 55, pp. 3551–3603, 2023, doi: 10.1007/s11063-022-11023-0.

[18] J. Yi, K. Tapia, J. W. Robinson, Z. Gandomkar, M. E. Suleiman, P. C. Brennan, N. Sommerfeld, and S. T. Taba, "Radiologists' performance in diagnosing silicosis on high-resolution computed tomography (HRCT) scans: An online platform," in *Medical Imaging 2024: Image Perception, Observer Performance, and Technology Assessment*, vol. 12929. Bellingham, WA, USA: SPIE, 2024, pp. 32–38, doi: 10.1117/12.3006114.

[19] G. K. Sharma, P. Harjule, B. Agarwal, and R. Kumar, "Silicosis detection using extended transfer learning model," in *Recent Trends in Image Processing and Pattern Recognition*. Cham, Switzerland: Springer, 2024, pp. 111–126, doi: 10.1007/978-3-031-53085-2_10.

[20] Y. Zhang, B. Zheng, F. Zeng, X. Cheng, T. Wu, Y. Peng, Y. Zhang, Y. Xie, W. Yi, W. Chen, J. Wu, and L. Li, "Potential of digital chest radiography-based deep learning in screening and diagnosing pneumoconiosis: An observational study," *Medicine*, vol. 103, no. 25, Art. no. e38478, 2024, doi: 10.1097/MD.0000000000038478.

[21] P. G. Anderson, H. Tarder-Stoll, M. Alpaslan, N. Keathley, D. L. Levin, S. Venkatesh, E. Bartel, S. Sicular, S. Howell, R. V. Lindsey, and R. M. Jones, "Deep learning improves physician accuracy in the comprehensive detection of abnormalities on chest X-rays," *Sci. Rep.*, vol. 14, Art. no. 25151, 2024, doi: 10.1038/s41598-024-76608-2.

[22] C. Liu, Y. Fang, Y. Xie, H. Zheng, X. Li, D. Wu, and T. Zhang, "Deep learning pneumoconiosis staging and diagnosis system based on multi-stage joint approach," *BMC Med. Imaging*, vol. 24, no. 1, Art. no. 165, 2024, doi: 10.1186/s12880-024-01337-x.

[23] B. Priego-Torres, D. Sanchez-Morillo, E. Khalili, M. Á. Conde-Sánchez, A. García-Gámez, and A. León-Jiménez, "Automated engineered-stone silicosis screening and staging using deep learning with X-rays," *Comput. Biol. Med.*, vol. 191, Art. no. 110153, 2025, doi: 10.1016/j.compbiomed.2025.110153.

[24] X. Li, M. Xu, Z. Yan, F. Xia, S. Li, Y. Zhang, Z. Xing, and L. Guan, "Deep convolutional network-based chest radiographs screening model for pneumoconiosis," *Front. Med.*, vol. 11, Art. no. 1290729, 2024, doi: 10.3389/fmed.2024.1290729.

[25] S. Hao, X. Li, W. Peng, Z. Fan, Z. Ji, and I. Ganchev, "YOLO-CXR: A novel detection network for locating multiple small lesions in chest X-ray images," *IEEE Access*, vol. 12, pp. 156003–156019, 2024, doi: 10.1109/ACCESS.2024.3482102.

[26] Z. Wang, J. Zhang, T. Wang, Z. Liu, W. Zhang, Y. Sun, X. Wu, H. Shao, and Z. Du, "The value of single biomarkers in the diagnosis of silicosis: A meta-analysis," *iScience*, vol. 27, no. 6, Art. no. 109948, 2024, doi: 10.1016/j.isci.2024.109948.

[27] W. Sun, D. Wu, Y. Luo, L. Liu, H. Zhang, S. Wu, Y. Zhang, C. Wang, H. Zheng, J. Shen, and C. Luo, "ExpertNet: Defeat noisy labels by deep expert consultation paradigm for pneumoconiosis staging on chest radiographs," *Expert Syst. Appl.*, vol. 232, Art. no. 120710, 2023, doi: 10.1016/j.eswa.2023.120710.

[28] L. Xiong, X. Liu, X. Qin, and W. Li, "Accurate pneumoconiosis staging via deep texture encoding and discriminative representation learning," *Front. Med.*, vol. 11, Art. no. 1440585, 2024, doi: 10.3389/fmed.2024.1440585.

[29] B. Priego-Torres, I. Sopo-Lambea, E. Khalili, A. Martín-Carrillo, A. Campos-Caro, A. León-Jiménez, and D. Sanchez-Morillo, "Multimodal fusion of chest X-rays and blood biomarkers for automated silicosis staging," *J. Clin. Med.*, vol. 14, no. 22, Art. no. 8074, 2025, doi: 10.3390/jcm14228074.